Lattice Boltzmann investigation on phase change of nanoparticle-enhanced phase change material in a cavity with separate plate

Yutao Huo, Zhonghao Rao[*]

School of Electrical and Power Engineering, China University of Mining and Technology, Xuzhou 221116, China

A B S T R A C T

The phase change material (PCM) can be used in thermal energy storage (TES) with large latent heat. However, due to the heat accumulation in the upper region, the solid-liquid phase change process will be slowed down. In this paper, in order to enhance the heat transfer of nanoparticle-enhanced PCM (NEPCM) in TES, a separate plate is applied to weaken the heat accumulation. The phase change multiple-relaxation-times lattice Boltzmann (MRT-LB) model is employed to solve the numerical problem and the effects of separate plate location, nanoparticle volume fraction and Rayleigh number are investigated. The results show that for all the Rayleigh numbers and volume fractions, the NEPCM of the case that separate plate is located in the middle of cavity melts fastest. Furthermore, the separate plate can reduce the temperature standard deviation. However, when the location of separate plate is less than 0.3, the melting process is slowed down, resulted from the heat accumulation near the separate plate.

1. Introduction

The thermal energy storage (TES) is important to energy-saving and emission-reduction. With large latent heat, the phase change material (PCM) has been used in TES [1]. However, the thermal conductivities of most of the PCMs are low, resulting in the slow heat transfer rate. There are two methods to enhance the heat transfer of PCM: (1) improving the thermal properties of PCM; (2) designing a more effective structure.

The nanoparticle with high thermal conductivity can be used to improve the thermal properties of PCM. Myers et al. [2] prepared the CuO nanoparticle-enhanced nitrate salt for TES. The thermal conductivity of nanoparticle-enhanced PCM (NEPCM) with 2 vol% CuO was increased by over 40%. The aqueous alumina nanofluids were prepared by Teng [3]. With 1.0 wt% Al_2O_3, the thermal conductivity of deionized water was increased by almost 10%. Karaipekli et al. [4] utilized the carbon nanotube to enhance the thermal conductivity of expanded perlite/paraffin composite. The solid-liquid phase change process of Al_2O_3/paraffin NEPCM in TES was revealed by Elbahjaoui and El Qarnia [5]. The melting time of NEPCM was much smaller than that of PCM. Mahamudur Rahman et al. [6] applied exfoliated graphene nanoplatelets to improve the thermal conductivity of PCM. With 4.5 wt % exfoliated graphene nanoplatelets, the melting time could be reduced by almost 60% when the diameter of cylinder was 14 mm.

Seddegh et al. [7] presented the heat charging and discharging processes numerically. When the TES unit was placed horizontally, the

total liquid fraction reached to 0.5 before 60 min. Then, the heat was accumulated in the upper region of unit and heat transfer was weakened. It took the PCM about 270 min to transform to liquid phase totally. The heat accumulation was obtained by Darzi et al. [8] in the melting process of NEPCM (Cu/water) as well. It is necessary to design an effective structure to enhance the heat transfer of PCM in the bottom region. Darzi et al. [9] employed the conductive fin to weaken the heat accumulation, and to improve the heat storage rate of TES. The heat could be transferred to the bottom PCM directly. The results showed that adopting 20 fins could reduce the melting time by almost 80%. The conductive fins were mounted on both the inner and outer cylinders in Ref. [1] and the melting time was reduced by 43.8%. Lohrasbi et al. [10] developed the radial fin and V-shaped fin to improve the thermal performance of TES. Based on the form of solid-liquid interface, the cold wall with curved surface in a cavity was proposed by Zhu et al. [11] to optimize the heat transfer of PCM in porous medium. In our previous work, the solid-liquid phase change process could be accelerated by using non-uniform heat flux distribution [12]. Darzi et al. [8] and Jourabian et al. [13] proved that the inner heater could be placed in the bottom part of the cavity to heat the bottom PCM directly.

As presented in Ref. [14], the spherical capsule was divided into two parts by the fin. The upward PCM flowed back after reaching to the fin. Consequently, the heat accumulation at the top was weakened and the melting process of PCM in the bottom region was accelerated. Based on this, the cavity with separate plate is developed to enhance the heat
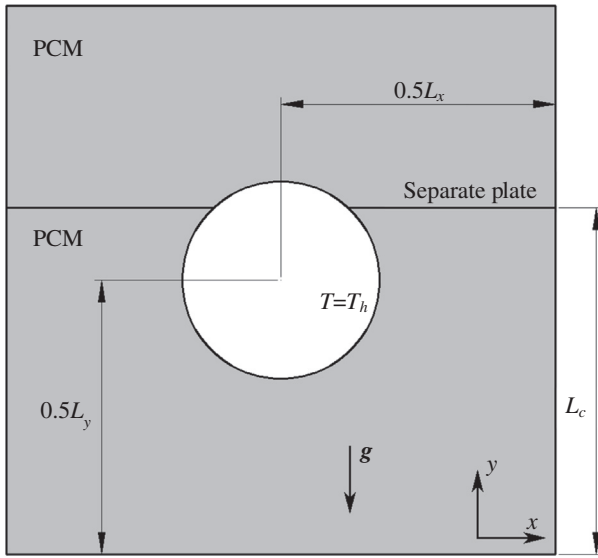
Fig. 1. Schematic of phase change in the cavity with a separate plane.

transfer of PCM in the bottom region in this paper. The effects of separate plate location, nanoparticle particle volume fraction and Rayleigh number are investigated.

2. Numerical method

2.1. Conservation equation

The schematic of solid-liquid phase change in a cavity with a separate plate is shown in Fig. 1. The aspect ratio of cavity is 1.0 and the length of the cavity is L. The cavity is filled with Al_2O_3 NEPCM. The inner cylinder is kept at high temperature, T_h, while the other walls are adiabatic. The radius of inner cylinder is R and R/L is 0.18. The NEPCM is at its phase change temperature, T_m, initially. The cavity is divided into two parts by an infinite thin separate plate, located at L_c and parallel to x-axis. Since the maximum volume faction of nanoparticle is less than 4% in this paper, the single phase model is applied and the NEPCM is assumed as incompressible, laminar and Newtonian [15]. The corresponding mass, momentum and energy conservation equations are given by [16]:

$$\nabla \cdot \boldsymbol{u} = 0 \tag{1}$$

$$\frac{\partial \boldsymbol{u}}{\partial t} + \nabla \cdot (\boldsymbol{uu}) = -\frac{1}{\rho_{nf}} \nabla p + \nabla \cdot (\nu_{nf} \nabla \boldsymbol{u}) + \boldsymbol{f}_m \tag{2}$$

$$\frac{\partial T}{\partial t} + \nabla \cdot (\boldsymbol{u}T) = \nabla \cdot (\alpha_{nf} \nabla T) - \left(\frac{h_{sl}}{C_p}\right)_{nf} \frac{\partial f_l}{\partial t} \tag{3}$$

where $\boldsymbol{u}$, t, ρ, p, C_p and T are velocity, time, density, pressure, specific heat at constant pressure and temperature of NEPCM, respectively. ν and α are the viscosity and thermal diffusivity. The subscripts, "nf" denotes "NEPCM". The viscosity and thermal diffusivity can be given by:

$$\nu_{nf} = \frac{\mu_{nf}}{\rho_{nf}} \tag{4}$$

$$\alpha_{nf} = \frac{\lambda_{nf}}{(\rho C_p)_{nf}} \tag{5}$$

where λ and μ are thermal conductivity and dynamic viscosity.

The third term on the right hand side of Eq. (2), $\boldsymbol{f}_m$, represents the body force and is derived from buoyancy in this paper. Based on the Boussinesq Assumption, the body force can be computed by [17]:

$$\boldsymbol{f}_m = -\boldsymbol{g}\beta_{nf}(T - T_{ref}) \tag{6}$$

where $\boldsymbol{g}$ is the acceleration of gravity and β_{nf} is thermal expansion of NEPCM. T_{ref} is the reference temperature and it is equal to the melting temperature of NEPCM in this paper.

The second term on the right hand side of Eq. (3) denotes the heat consumed by phase change and h_{sl} is the latent heat. f_l is liquid fraction ($f_l = 0$: solid; $f_l = 1$: liquid; $0 < f_l < 1$: mushy zone). The total enthalpy, H, can be derived from Eq. (3) and defined as:

$$H = (C_p)_{nf} T + (h_{sl})_{nf} f_l \tag{7}$$

The temperature and liquid fraction can be determined by the enthalpy:

$$T = \begin{cases} \frac{H}{(C_p)_{nf}} & H < H_s \\ T_s + \frac{H - H_s}{H_l - H_s}(T_l - T_s) & H_s \leqslant H < H_l \\ T_l + \frac{(H - H_l)}{(C_p)_{nf}} & H \geqslant H_l \end{cases} \tag{8}$$

$$f_l = \begin{cases} 0 & H < H_s \\ \frac{H - H_s}{H_l - H_s} & H_s \leqslant H < H_l \\ 1 & H \geqslant H_l \end{cases} \tag{9}$$

where T_s and H_s are the solidus temperature and enthalpy. T_l and H_l are the liquidus temperature and enthalpy. In this paper, the thermal properties of solid phase equal that of liquid phase with $T_m = T_s = T_l$ [5].

The thermal properties of PCM and nanoparticle are shown in Table 1. The density, heat capacity, thermal expansion and latent heat of NEPCM are computed by [18]:

$$\rho_{nf} = (1-\phi)\rho_f + \phi\rho_p \tag{10}$$

$$(\rho C_p)_{nf} = (1-\phi)(\rho C_p)_f + \phi(\rho C_p)_p \tag{11}$$

$$(\rho\beta)_{nf} = (1-\phi)(\rho\beta)_f \tag{12}$$

$$(\rho h_{sl})_{nf} = (1-\phi)(\rho h_{sl})_f \tag{13}$$

where the subscripts "f" and "p" represent "PCM" and "nanoparticle". ϕ is the volume fraction of nanoparticle. The dynamic viscosity of NECPM, μ_{nf} is given by [18]:

$$\mu_{nf} = 0.983\mu_f \exp(12.959\phi) \tag{14}$$

The Maxwell-Garnetts model is adopted to obtain the thermal conductivity of NEPCM [19,20]:

$$\lambda_{nf} = \frac{\lambda_p + 2\lambda_f + 2(\lambda_p - \lambda_f)\phi}{\lambda_p + 2\lambda_f - 2(\lambda_p - \lambda_f)\phi}\lambda_f \tag{15}$$

In order to further analyze, the dimensionless forms of conservation equations are developed:
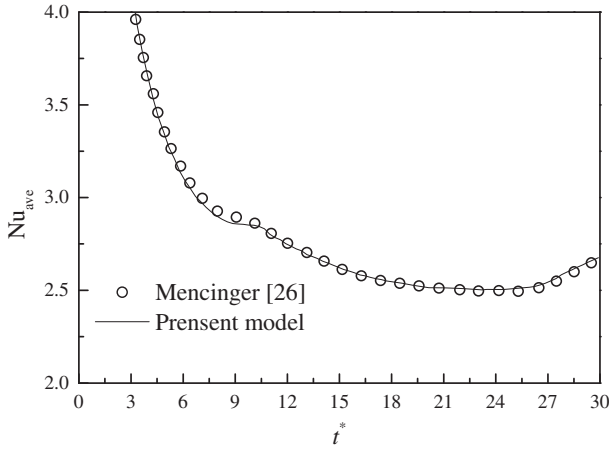
$$\nabla^* \cdot \boldsymbol{u}^* = 0 \tag{16}$$

$$\frac{\partial \boldsymbol{u}^*}{\partial t^*} + \sqrt{RaPr}\, \nabla^* \cdot (\boldsymbol{u}^* \boldsymbol{u}^*) = -\frac{1}{\psi_\rho} \nabla^* p^* + Pr\psi_\nu \nabla^* \cdot (\nabla^* \boldsymbol{u}^*) - \psi_\beta T^* \boldsymbol{n}_g \sqrt{RaPr} \tag{17}$$

$$\frac{\partial T^*}{\partial t^*} + \sqrt{RaPr}\, \nabla^* \cdot (\boldsymbol{u}^* T^*) = \psi_\alpha \nabla^* \cdot (\nabla^* T^*) + \frac{\psi_h}{\psi_C}\frac{1}{Ste}\frac{\partial f_l}{\partial t^*} \tag{18}$$
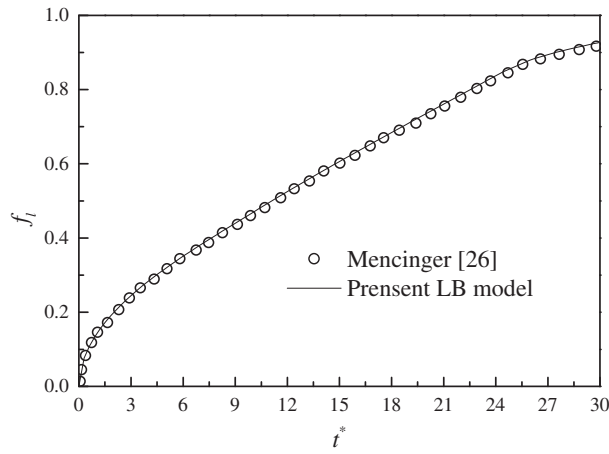
with:

Table 1
Thermal properties of PCM and nanoparticle.

	ρ	C_p	λ	μ	h_{sl}
PCM/paraffin	930	1600	0.21	9.2×10^{-4}	195000
Al_2O_3 nanoparticles	3880	765	25	–	–

(a)

Fig. 3. The grid independence test.

(b)

Fig. 2. The comparisons of (a) average Nusselt number and (b) total liquid fraction between present model and Mencinger's work.

$$T^* = \frac{T - T_c}{T_h - T_c}, \quad t^* = \frac{\alpha_f t}{L^2}, \quad \nabla^* = L\nabla, \quad \boldsymbol{u}^* = \frac{\boldsymbol{u}}{U},$$
$$U = \sqrt{g\beta_f(T_h - T_m)L}, \quad p^* = \frac{p}{\rho_f \alpha_f U} \tag{19}$$

$\boldsymbol{n}_g$ is the unit vector in the direction of gravity. The Prandtl number, Rayleigh number and Stefan number are determined by:

$$\text{Pr} = \frac{\nu_f}{\alpha_f}, \quad \text{Ra} = \left(\frac{\beta}{\nu\alpha}\right)_f (T_h - T_m)gL^3, \quad \text{Ste} = \left(\frac{C_p}{h_{sl}}\right)_f \Delta T \tag{20}$$

It is noted that as shown in Eqs. (18) and (19), all the dimensionless properties are derived from the properties of PCM. The ratios of properties between NEPCM and PCM are defined as:

$$\psi_\alpha = \frac{\alpha_{nf}}{\alpha_f}, \quad \psi_\nu = \frac{\nu_{nf}}{\nu_f}, \quad \psi_\rho = \frac{\rho_{nf}}{\rho_f}, \quad \psi_\beta = \frac{\beta_{nf}}{\beta_f}, \quad \psi_h = \frac{(h_{sl})_{nf}}{(h_{sl})_f}, \quad \psi_C = \frac{(C_p)_{nf}}{(C_p)_f} \tag{21}$$

2.2. Lattice Boltzmann model

In this paper, the total-enthalpy based MRT-LB is applied to solve the numerical model. As reported in Ref. [21], the phase interface effects in single-relaxation-time LB (SRT-LB) lead to inaccurate results near solid-liquid interface. H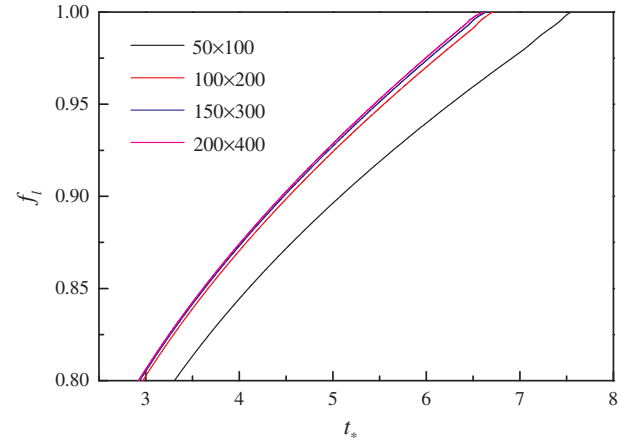owever, the phase interface effects can be removed in MRT-LB. The evolution equations of density and total enthalpy distribution functions are given by [21]:

$$\boldsymbol{f}(\boldsymbol{x} + \boldsymbol{e}\Delta t, t + \Delta t) = \boldsymbol{f}(\boldsymbol{x}, t) - \boldsymbol{M}^{-1}\boldsymbol{S}\left[\boldsymbol{m}(\boldsymbol{x}, t) - \boldsymbol{m}^{eq}(\boldsymbol{x}, t)\right]$$
$$+ \Delta t\boldsymbol{M}^{-1}\left(\boldsymbol{I} - \frac{\boldsymbol{S}}{2}\right)\boldsymbol{F}_m(\boldsymbol{x}, t) \tag{22}$$

$$\boldsymbol{g}(\boldsymbol{x} + \boldsymbol{e}\Delta t, t + \Delta t) = \boldsymbol{g}(\boldsymbol{x}, t) - \boldsymbol{M}^{-1}\boldsymbol{R}\left[\boldsymbol{n}(\boldsymbol{x}, t) - \boldsymbol{n}^{eq}(\boldsymbol{x}, t)\right] \tag{23}$$

with:

$$\boldsymbol{f}(\boldsymbol{x} + \boldsymbol{e}\Delta t, t + \Delta t) = [f_0(\boldsymbol{x} + \boldsymbol{e}_0\Delta t, t + \Delta t), \cdots, f_8(\boldsymbol{x} + \boldsymbol{e}_8\Delta t, t + \Delta t)]^\mathrm{T} \tag{24}$$

$$\boldsymbol{g}(\boldsymbol{x} + \boldsymbol{e}\Delta t, t + \Delta t) = [g_0(\boldsymbol{x} + \boldsymbol{e}_0\Delta t, t + \Delta t), \cdots, g_8(\boldsymbol{x} + \boldsymbol{e}_8\Delta t, t + \Delta t)]^\mathrm{T} \tag{25}$$

The D2Q9 model is applied in this paper, with which there are 9 discrete velocities:

$$\boldsymbol{e}_i = \begin{cases} (0,0) & i = 0 \\ c\left(\cos\left[\frac{\pi}{2}(i-1)\right], \sin\left[\frac{\pi}{2}(i-1)\right]\right) & i = 1,2,3,4 \\ \sqrt{2}c\left(\cos\left[\frac{\pi}{4}(2i-1)\right], \sin\left[\frac{\pi}{4}(2i-1)\right]\right) & i = 5,6,7,8 \end{cases} \tag{26}$$

where $c = \Delta x/\Delta t$ is the lattice speed.

The transformation matrix, $\boldsymbol{M}$, is expressed as [22]:

$$\boldsymbol{M} = \begin{pmatrix} 1 & 1 & 1 & 1 & 1 & 1 & 1 & 1 & 1 \\ -4 & -1 & -1 & -1 & -1 & 2 & 2 & 2 & 2 \\ 4 & -2 & -2 & -2 & -2 & 1 & 1 & 1 & 1 \\ 0 & 1 & 0 & -1 & 0 & 1 & -1 & -1 & 1 \\ 0 & -2 & 0 & 2 & 0 & 1 & -1 & -1 & 1 \\ 0 & 0 & 1 & 0 & -1 & 1 & 1 & -1 & -1 \\ 0 & 0 & -2 & 0 & 2 & 1 & 1 & -1 & -1 \\ 0 & 1 & -1 & 1 & -1 & 0 & 0 & 0 & 0 \\ 0 & 0 & 0 & 0 & 0 & 1 & -1 & 1 & -1 \end{pmatrix} \tag{27}$$

$\boldsymbol{m}(\boldsymbol{x}, t) = \boldsymbol{M}\boldsymbol{f}(\boldsymbol{x}, t)$ and $\boldsymbol{n}(\boldsymbol{x}, t) = \boldsymbol{M}\boldsymbol{g}(\boldsymbol{x}, t)$ are the rescaled moments. Similarly, the equilibrium moments are defined as:

$$\boldsymbol{m}^{eq}(\boldsymbol{x}, t) = \boldsymbol{M}\boldsymbol{f}^{eq}(\boldsymbol{x}, t)$$
$$= \left(\rho, -2\rho + 3\rho_0\frac{\boldsymbol{u}^2}{c^2}, \rho - 3\rho_0\frac{\boldsymbol{u}^2}{c^2}, \rho_0\frac{u_x}{c}, -\rho_0\frac{u_x}{c}, \rho_0\frac{u_y}{c}, -\rho_0\frac{u_y}{c}, \rho_0\frac{u_x^2 - u_y^2}{c}, \rho_0\frac{u_x u_y}{c^2}\right)^\mathrm{T} \tag{28}$$
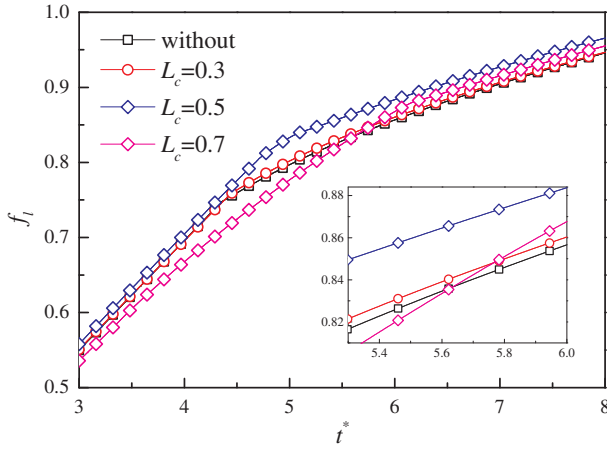
Fig. 4. Variations of total liquid fraction for pure PCM.

$$n^{eq}(\boldsymbol{x},t) = \boldsymbol{M}g^{eq}(\boldsymbol{x},t)$$

$$= \left(H, -4H + 2C_pT + 3C_pT\frac{\boldsymbol{u}^2}{c^2}, 4H - 3C_pT - 3C_pT\frac{\boldsymbol{u}^2}{c^2}, C_pT\frac{u_x}{c}, \right.$$

$$\left. -C_pT\frac{u_x}{c}, C_pT\frac{u_y}{c}, -C_pT\frac{u_y}{c}, C_pT\frac{u_x^2-u_y^2}{c^2}, C_pT\frac{u_xu_y}{c^2} \right)^{\mathrm{T}}$$

(29)

where ρ_0 is the mean density. $\boldsymbol{I}$ in Eq. (22) is the unit matrix. $\boldsymbol{F}_m$ is the discrete force term in moment space, given by:

$$\boldsymbol{F}_m(\boldsymbol{x},t) = \left(0, 6\rho_0\frac{\boldsymbol{f}_m\cdot\boldsymbol{u}}{c^2} - 6\rho_0\frac{\boldsymbol{f}_m\cdot\boldsymbol{u}}{c^2}, \rho_0\frac{f_{mx}}{c}, -\rho_0\frac{f_{mx}}{c}, \rho_0\frac{f_{my}}{c}, \right.$$

$$\left. -\rho_0\frac{f_{my}}{c}, 2\rho_0\frac{f_{mx}u_x-f_{my}u_y}{c^2}, \rho_0\frac{f_{mx}u_y+f_{my}u_x}{c^2} \right)^{\mathrm{T}}$$

(30)

Then, the macroscopic quantities are calculated by:

$$\rho = \sum_i f_i$$

(31)

$$\rho_0\boldsymbol{u} = \sum_i \boldsymbol{e}_if_i + \frac{\Delta t}{2}\rho_0\boldsymbol{f}_m$$

(32)

$$H = \sum_i g_i$$

(33)

$\boldsymbol{S}$ and $\boldsymbol{R}$ in Eqs. (22) and (23) are the diagonal relaxation matrixes, as follows:

$$\boldsymbol{S} = \mathrm{diag}(s_0, s_e, s_\varepsilon, s_j, s_q, s_j, s_q, s_\nu, s_\nu)$$

(34)

$$\boldsymbol{R} = \mathrm{diag}(r_0, r_e, r_\varepsilon, r_j, r_q, r_j, r_q, r_e, r_e)$$

(35)

with $s_0 = s_j = r_0 = 1$, $s_\nu = 1/\tau_f$, $r_j = 1/\tau_g$ and $0 < s_{e,\varepsilon,q}, r_{e,\varepsilon,q} < 2$. Furthermore, the following restriction needs to be guaranteed [21]:

$$\left(\frac{1}{r_e} - \frac{1}{2}\right)\left(\frac{1}{r_j} - \frac{1}{2}\right) \equiv \frac{1}{4}$$

(36)

Since the rigid square mesh is applied in MRT-LB, the ghost fluid boundary condition is adopted on the curved boundary condition (inner cylinder in Fig. 1). The distribution function is divided into two parts:
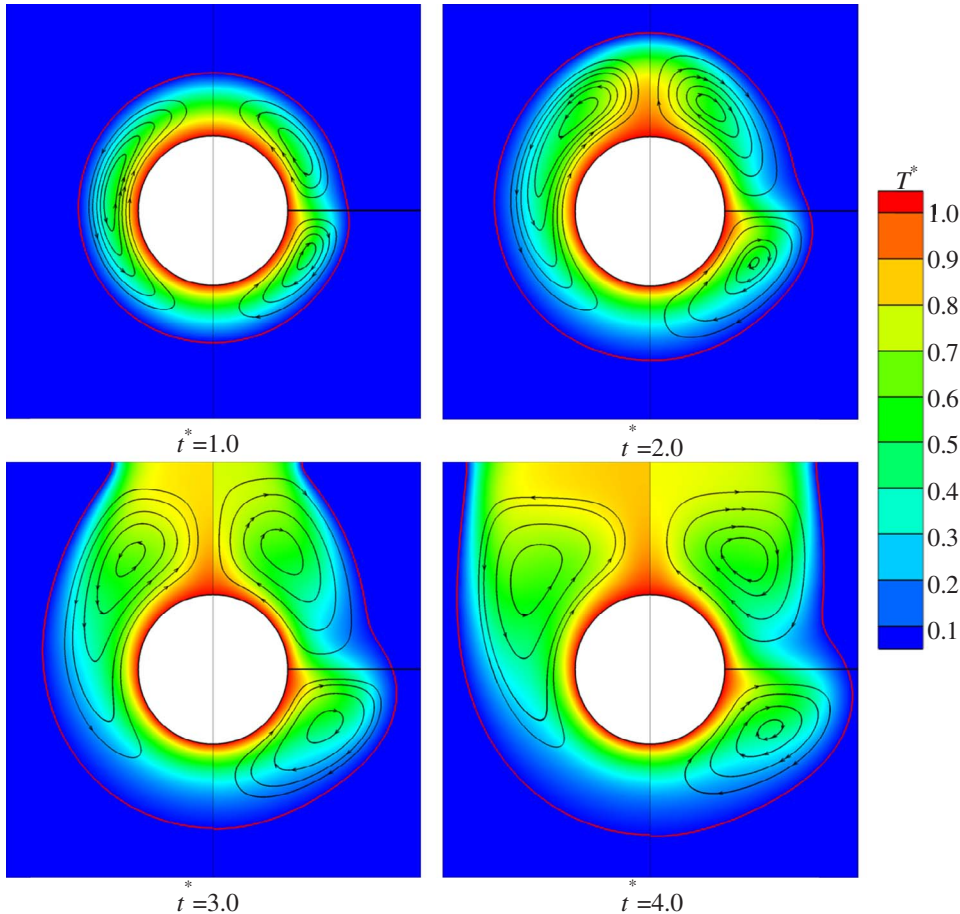
Fig. 5. Temperature contours at different moments for pure PCM (Left half part: without separate plate, right half part: $L_c = 0.5$).

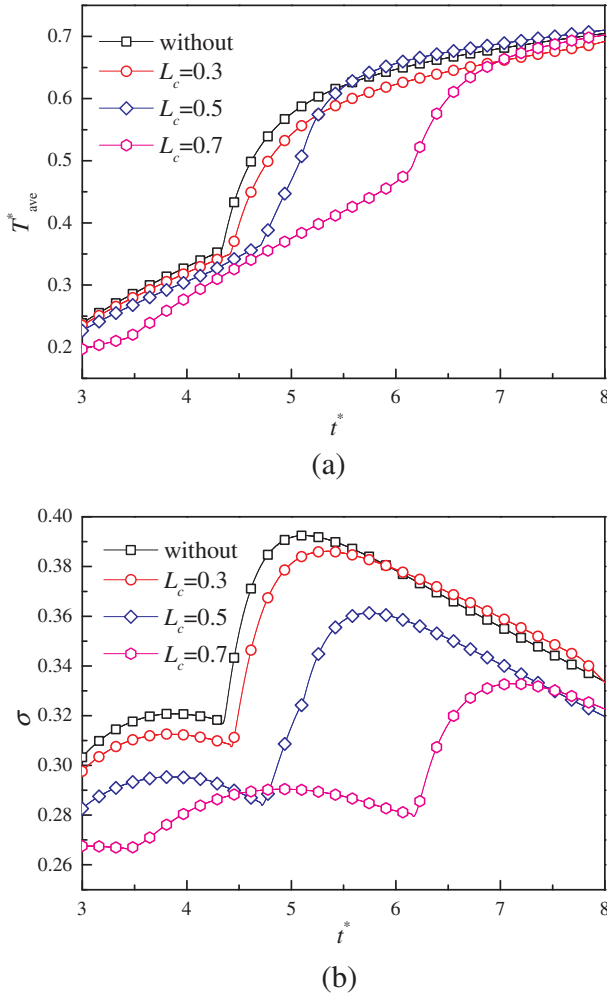Red solid line: solid-liquid interface

Black solid line: streamline

(a)

(b)

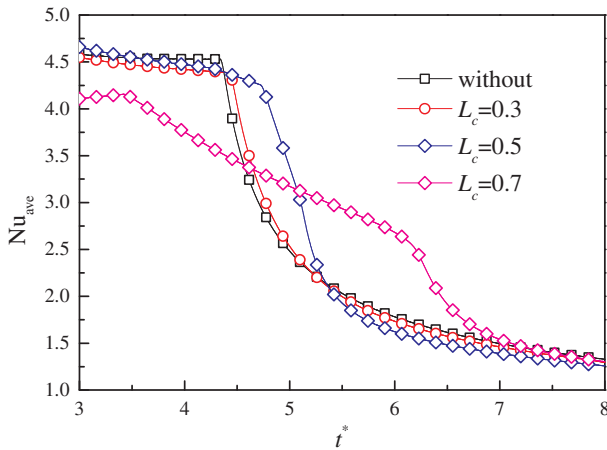**Fig. 6.** Variations of (a) average temperature and (b) temperature standard deviation for pure PCM.

Fig. 7. Variations of average Nusselt number for pure PCM.

the equilibrium part and non-equilibrium part. The equilibrium part is computed by:

$$\boldsymbol{f}^{eq} = (f_0^{eq}, f_1^{eq}, f_2^{eq}, f_3^{eq}, f_4^{eq}, f_5^{eq}, f_6^{eq}, f_7^{eq}, f_8^{eq})^T \tag{37}$$

$$f_i^{eq} = \omega_i \rho + \omega_i \rho_0 \left[\frac{\boldsymbol{e}_i \cdot \boldsymbol{u}}{c_s^2} + \frac{(\boldsymbol{e}_i \cdot \boldsymbol{u})^2}{2c_s^4} - \frac{u^2}{2c_s^2} \right] \tag{38}$$
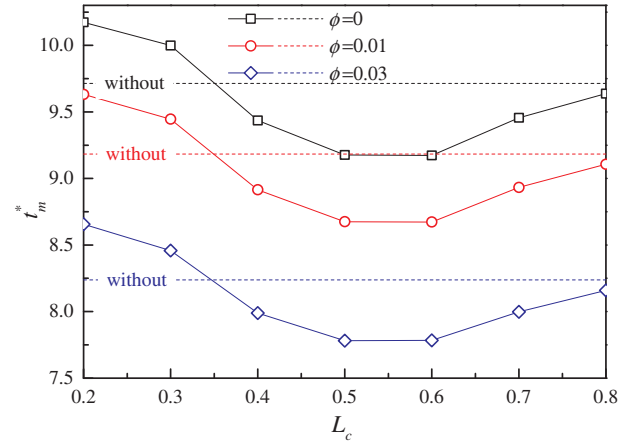

Fig. 8. Melting times of NEPCM with different volume fractions.

$$\boldsymbol{g}^{eq} = (g_0^{eq}, g_1^{eq}, g_2^{eq}, g_3^{eq}, g_4^{eq}, g_5^{eq}, g_6^{eq}, g_7^{eq}, g_8^{eq})^T \tag{39}$$

$$g_i^{eq} = \begin{cases} H - C_p T + \omega_i C_p T \left(1 - \frac{u^2}{2c_s^2}\right) & i = 0 \\ \omega_i C_p T \left[1 + \frac{\boldsymbol{e}_i \cdot \boldsymbol{u}}{c_s^2} + \frac{(\boldsymbol{e}_i \cdot \boldsymbol{u})^2}{2c_s^4} - \frac{u^2}{2c_s^2} \right] & i \neq 0 \end{cases} \tag{40}$$

where ω_i is the weighting coefficient:

$$\omega_i = \begin{cases} \frac{4}{9} & i = 0 \\ \frac{1}{9} & i = 1,2,3,4 \\ \frac{1}{36} & i = 5,6,7,8 \end{cases} \tag{41}$$

The macroscopic quantities and the non-equilibrium part are computed by interpolation, and the detailed information can be found in Ref. [23]. The non-equilibrium extrapolation scheme proposed by Guo et al. [24] is applied to the walls of cavity and separate plate. In this scheme, the distribution function is divided into two parts as well. The unknown non-equilibrium part is derived the node adjacent to the boundary. As mentioned above, the separate plate is infinitely thin and the material is assumed as stable PCM. Consequently, the macroscopic quantities on the separate plate can be determined by the adjacent node as well.

It is noted that all the properties in this sub-section are of NEPCM and the subscript "*nf*" is omitted for convenience. The dimensionless relaxation times, τ_f and τ_g, are defined as:

$$\tau_f = 3\frac{\nu_{nf}}{c^2 \Delta t} + 0.5 \tag{42}$$

$$\tau_g = 3\frac{\alpha_{nf}}{c^2 \Delta t} + 0.5 \tag{43}$$

The average temperature and temperature standard deviation of NEPCM are defined as:

$$T_{ave}^* = \frac{\int_S T^* dS}{\int_S dS} \tag{44}$$

$$\sigma = \sqrt{\frac{\int_S (T^* - T_{ave}^*)^2 dS}{\int_S dS}} \tag{45}$$

where S denotes the area of enclosure.

The surface-averaged Nusselt number is obtained by:

$$Nu = \frac{1}{2\pi} \int_{-\pi}^{\pi} L\left(\frac{\partial T^*}{\partial \boldsymbol{n}}\right) d\theta \tag{46}$$

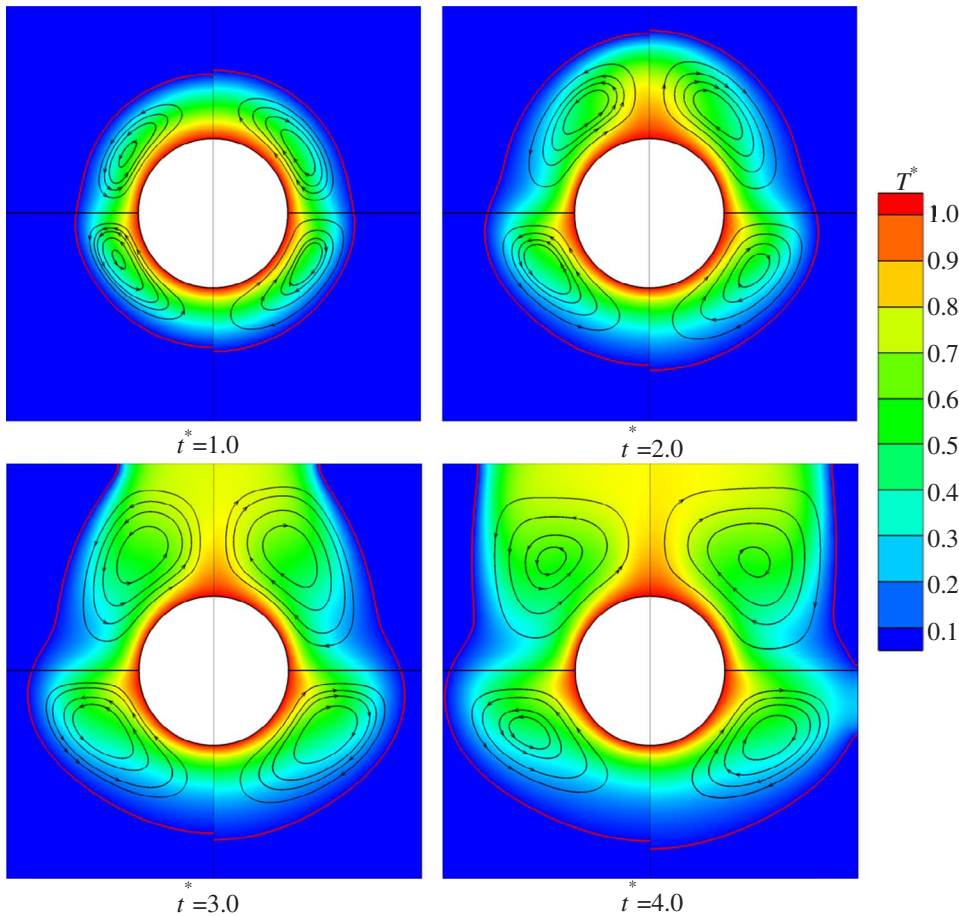where $\boldsymbol{n}$ is the unit outer-normal vector of inner cylindrical wall and θ represents the angle.

Fig. 9. Temperature contours at different moments for NEPCM ($L_c = 0.5$, Left half part: $\phi = 0.01$, right half part: $\phi = 0.03$).

$t^* = 1.0$

$t^* = 2.0$

$t^* = 3.0$

$t^* = 4.0$

Red solid line: solid-liquid interface

Black solid line: streamline

2.3. Verification

In this sub-section, the present numerical model is verified firstly. The problem of solid-liquid phase change in a cavity is solved by the present model and the results are compared with that of benchmark solution reported in Ref. [25]. The comparisons of average Nusselt number and total liquid fraction are presented in Fig. 2. The results agree well with that of Mencinger. Moreover, the mesh independent test is conducted as well. It is noted that since the cavity is bilateral symmetrical, only half part of the cavity is simulated. For all the simulations, the Mach number ($Ma = U/c_s$) is set as 0.1 to compute the viscosity and thermal diffusivity. The Ra is 10^5 (the largest Ra in this paper) and ϕ is 0.03 with $L_c = 0.5$ in grid independence test. The mesh systems ($x \times y$) of 50×100, 100×200, 150×300 and 200×400 are considered and the results are presented in Fig. 3. The melting times are 7.55, 6.72, 6.64 and 6.61, respectively. The relative differences between mesh systems of 150×300 and 200×400 is less than 1%. Consequently, the mesh system of 150×300 is applied in this paper.

3. Results and discussions

3.1. Effects of location

In this sub-section, the effects of separate plate location are investigated. The Rayleigh number is fixed at 10^4 and the volume fraction is set as 0 (pure PCM). The Stefan number is kept as 0.1 in this subsection. The variations of total liquid fraction with different locations of plate are shown in Fig. 4. It can be obtained that the PCM with $L_c = 0.5$ melts most quickly. As mentioned before, the melting rate in the last

stage is slow, resulted from the heat accumulation in upper region of cavity. For example, without separate plate, the increase rate of total liquid fraction (slope of curve in Fig. 4) is 0.05 after $t^* = 4.5$ for pure PCM, while the increase rate is almost 0.2 before $t^* = 4.5$. However, with $L_c = 0.5$, the increase rate of total liquid fraction is reduced at near $t^* = 5.0$. The phenomenon is on account of the flow divided by separate plate, as shown in Fig. 5. In Fig. 5, the left half part of cavity represents the case without separate plate while the right half part denotes the one with $L_c = 0.5$. Apparently, driven by the buoyancy, the heated PCM flows upwards near the inner cylinder and downwards near the solid-liquid interface. Then, the convection circulation is formed. However, the separate plate obstructs the upward PCM flow and divides the cavity into two parts. The PCM in the bottom part flows downwards after it reaches to the plate. As a result, the heat accumulation is weakened and the PCM melts faster, as shown in Fig. 4. Furthermore, with $L_c = 0.3$, the PCM melts faster than that without separate plate. However, when L_c is increased to 0.7, the melting process is slowed down in the initial stage. Then, as mentioned above, the decrease of slope is delayed and the total liquid fraction with $L_c = 0.7$ catches up with that without separate plate.

The variations of average temperature and temperature standard deviation are shown in Fig. 6. Since more heat is used to phase change, the average temperature of case with $L_c = 0.3$ is smaller than that of the one without separate plate, as presented in Fig. 6(a). The same phenomenon can be obtained from the case with $L_c = 0.5$ before $t^* = 5.5$ as well. Then, due to the accelerated heat transfer rate, the average temperature with $L_c = 0.5$ is the largest in the last stage. As shown in Fig. 5, the heat is accumulated in the upper region of cavity in case without plate, which enlarges the temperature non-uniformity, σ. It
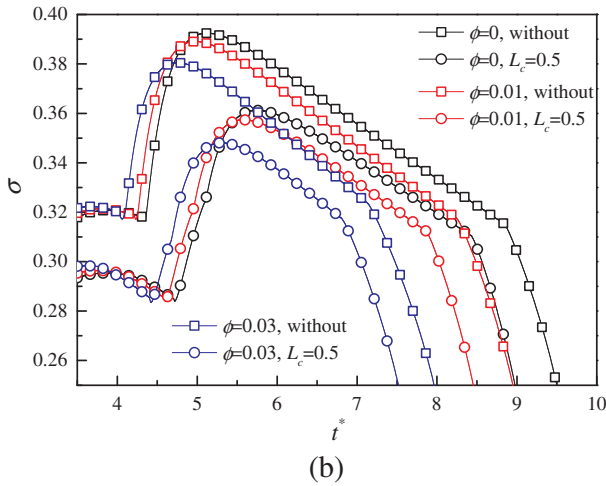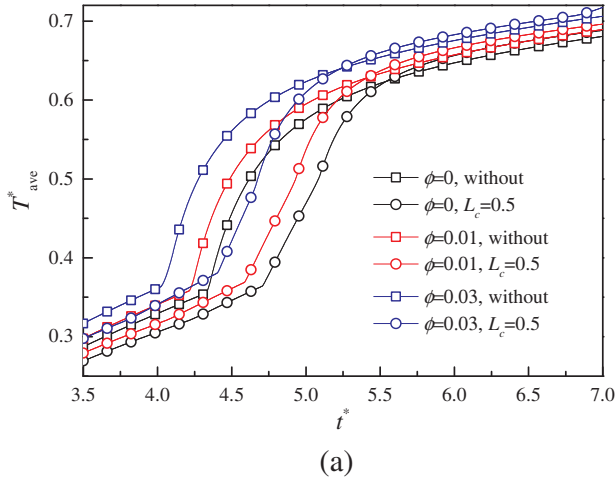
(a)

(b)

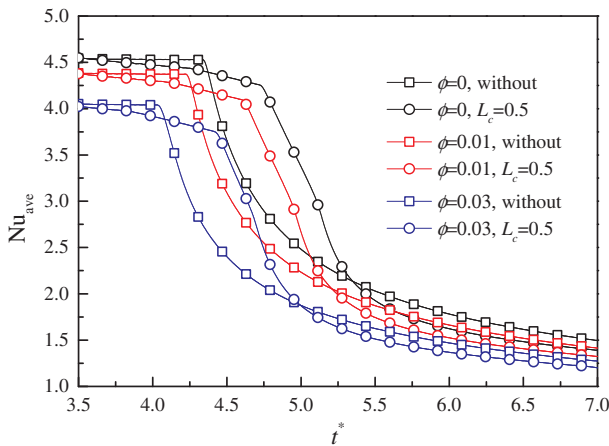**Fig. 10.** Variations of (a) average temperature and (b) temperature standard deviation for NEPCM.

Fig. 11. Variations of average Nusselt number for NEPCM.

Fig. 12. Melting times of NEPCM with different Rayleigh numbers ($\phi = 0.03$).

Fig. 13. Variations of total liquid fraction for NEPCM ($\phi = 0.03$).

demonstrates that separate plate is able to get the temperature distribution more uniform. When the separate plate moves from 0.5 to 0.7, the heat transfer rate is slowed down. The difference of temperature rise is decreased and the temperature standard deviation is reduced.

The variations of average Nusselt number are shown in Fig. 7. As shown in Eq. (46), the Nusselt number denotes the rate of heat transferred from the inner cylinder. Once again, resulted from the flow division of separate plate, the decrease rate of Nusselt number with
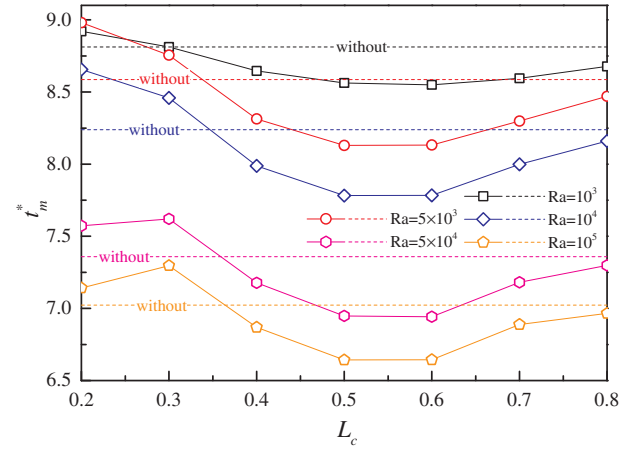
separate plate is smaller than the case without plate. Furthermore, in the last stage, the Nusselt number of the case with $L_c = 0.5$ is minimum. It leads to the slower increase rate of total liquid fraction. However, since more PCM is transformed to liquid phase, the input energy after $t^* = 4.5$ is mostly used for sensible heat, leading to the quick increase of average temperature in Fig. 6.

3.2. Effects of volume fraction

In this sub-section, the effects of nanoparticle volume fraction are investigated. The Stefan number is set as 0.1. The melting times, t_m^* (NEPCM transforms to liquid phase totally) with different volume fractions and locations of separate plate are shown in Fig. 8. For all the volume fractions, when L_c is larger than 0.3, the solid-liquid phase change processes are accelerated. It is noted that compared with the case without separate plate, the melting times of $L_c = 0.5$ are reduced by 0.0553, 0.0554 and 0.0554, for volume fractions of 0, 0.01 and 0.03, respectively. It demonstrates that the separate plate leads to the approximate effects on PCM and NEPCM. However, when L_c is less than 0.3, the heat transfer is weakened. It takes $t^* = 8.6562$ to transform 3 vol % NEPCM from solid phase to liquid phase totally when L_c is 0.2. However, for the same material, the melting time is 8.2382 without separate plate. As shown in Fig. 9, the cavity is divided into two parts, the upper part and bottom one, by the separate plate. As mentioned above, R/L is 0.18. Namely, the cylinder is located at $y^* \in [0.32, 0.68]$. It is noted that the natural convection is the circulation and the high-temperature NEPCM flows upwards. When L_c is 0.3 or 0.2, the NEPCM
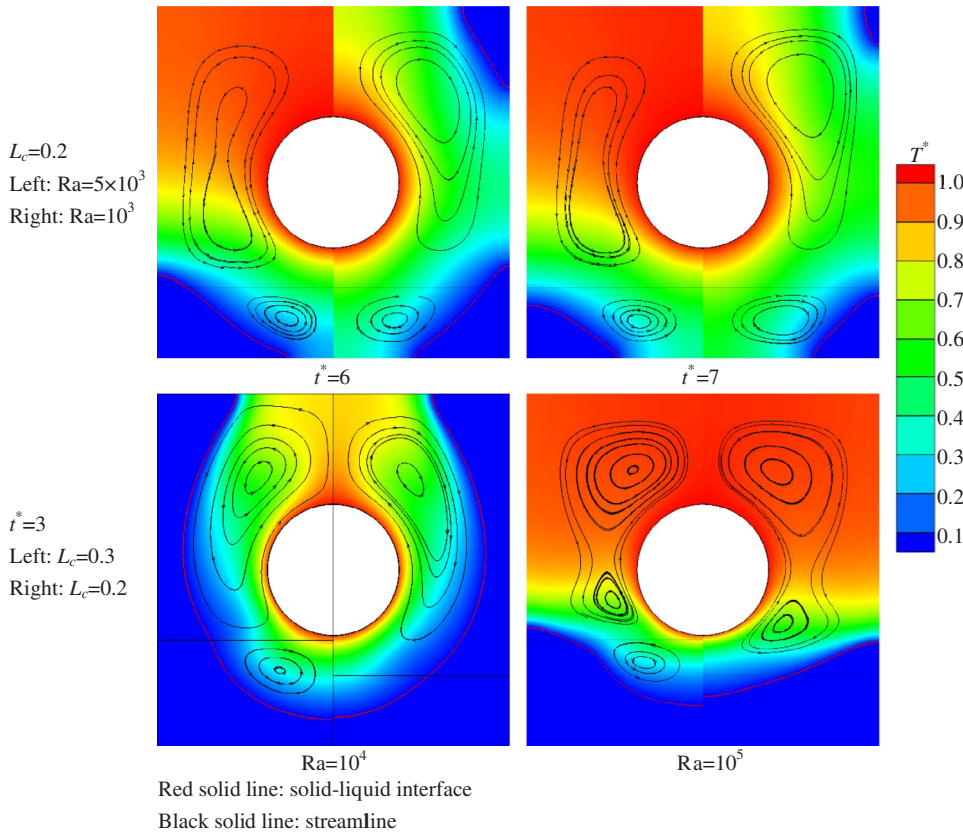
Fig. 14. Temperature contours at different moments for NEPCM with 3 vol% nanoparticle.

$L_c=0.2$
Left: Ra=5×10^3
Right: Ra=10^3

$t^*=3$
Left: $L_c=0.3$
Right: $L_c=0.2$

$t^*=6$ $t^*=7$

Ra=10^4 Ra=10^5

Red solid line: solid-liquid interface
Black solid line: streamline

in bottom part is heated by the upper part and the energy is transferred through the separate plate. As the heat accumulation in at the top of cavity, the heat is accumulated near the separate plate. Consequently, the heat transfer through the plate is weakened and the melting process of bottom part is slowed down. When L_c is 0.7 or 0.8, the upper part is heated by the bottom part. It is noted that the heat transfer rate of upper part is slow as well since the distance between upper wall (phase interface) and separate plate is short. In the meanwhile, the NEPCM is heated by the cylinder directly and melts more quickly. As a result, when L_c is 0.7 or 0.8, the melting process is accelerated slightly.

Furthermore, increasing the volume fraction can enhance the heat transfer as well, as shown in Fig. 9. The left half part presents the temperature contour and streamlines of NEPCM with 1 vol% nanoparticle, while the right half part is of NEPCM with 3 vol% nanoparticle. The contours prove that with the higher volume fraction of nanoparticle, the solid-liquid interface moves faster. Namely, the higher volume fraction leads to smaller melting time, as shown in Fig. 8. With $L_c = 0.5$, when the volume fraction is increased from 0.01 to 0.03, the melting time is reduced by over 10%. Fig. 10 presents the variations of average temperature and temperature standard deviation. As mentioned in Section 3.1, in the first stage, more heat is applied to transform NEPCM to liquid phase, leading to faster melting rate (Fig. 8) and smaller average temperature, as shown in Fig. 10(a). Resulted from the enhanced heat transfer by separate plate, the average temperature with $L_c = 0.5$ catches up with that without separate plate. Moreover, this phenomenon is more obvious when the volume fraction of nanoparticle is increased. The coincidence points of average temperature between the case with $L_c = 0.5$ and without separate plate are located at t^* of 5.22, 5.44 and 5.59, for pure PCM, NEPCM with 1 vol% and 3 vol% nanoparticle, respectively. The temperature standard deviation with $L_c = 0.5$ decreases a lot after $t^* = 5$ for pure PCM. As shown in Fig. 4, the increment rate of total liquid fraction decreases after $t^* = 5$ as well, resulted from the heat accumulation. As shown in Fig. 10(b), increasing the volume fraction of nanoparticle will advance this process. Although raising the volume fraction can increase the temperature standard

deviation in the first stage, the temperature distribution of NEPCM becomes more uniform since the melting process is advanced. As shown in Fig. 11, the average Nusselt number with $L_c = 0.5$ decreases a lot after $t^* = 4.73$ for pure PCM. However, for 3 vol% NEPCM, the inflection point is located at $t^* = 4.43$.

3.3. Effects of Rayleigh number

In this sub-section, the effects of Rayleigh number on the phase change process of NEPCM with $\phi = 0.03$ are investigated. The Stefan number is set as 0.1. The melting times of NEPCM with different Rayleigh numbers are shown in Fig. 12. For all the Rayleigh numbers, when L_c is larger than 0.3, the separate plate will accelerate the melting process. To the contrary, with $L_c < 0.3$, the separate plate leads to larger melting time. However, with $L_c = 0.2$, when the Rayleigh number is increased from 10^3 to 5×10^3, the melting time is increased from 8.9200 to 8.9806. Keeping increasing the Rayleigh number can decrease the melting time, and leads to faster solid-liquid phase change. The variations of total liquid fraction for NEPCM are shown in Fig. 13. When L_c is 0.2, the melting rate of the case with Ra = 10^3 is slower than that of the case with Ra = 5×10^3 before $t^* = 6.85$. Then the total liquid fraction of the case with Ra = 10^3 catches up with the case with Ra = 5×10^3. The temperature contours and streamlines can be obtained in Fig. 14. As can be seem, when the dimensionless time is 6, most of the NEPCM in the upper part of the case with Ra = 5×10^3 transforms to liquid phase. Consequently, the heat accumulation mentioned above leads to the slower melting rate, as the variation of total liquid fraction after $t^* = 4.7$ in Fig. 13. From $t^* = 6$ to $t^* = 7$, the melting zone of the case with Ra = 5×10^3 varies a little, as shown in Fig. 14. However, for the case with Ra = 10^3, resulted from the lower Ra, the melting rate is smaller than that of the case with Ra = 5×10^3, initially. As shown in Eq. (20), the smaller Ra leads to weaker natural convection, slower heat transfer rate and smaller average temperature shown in Fig. 15(a). As a result, the heat accumulation is weakened and the temperature distributes more uniform (smaller
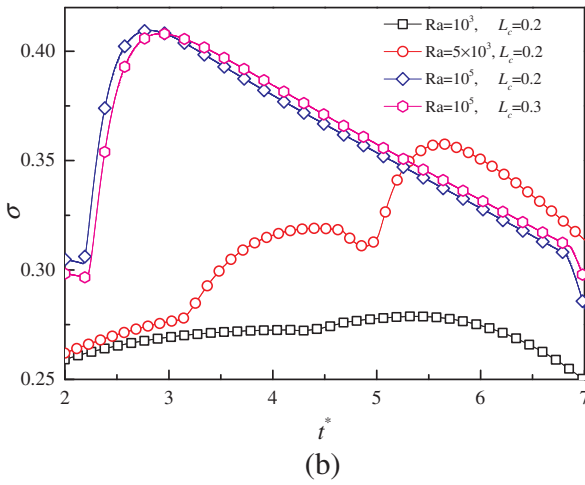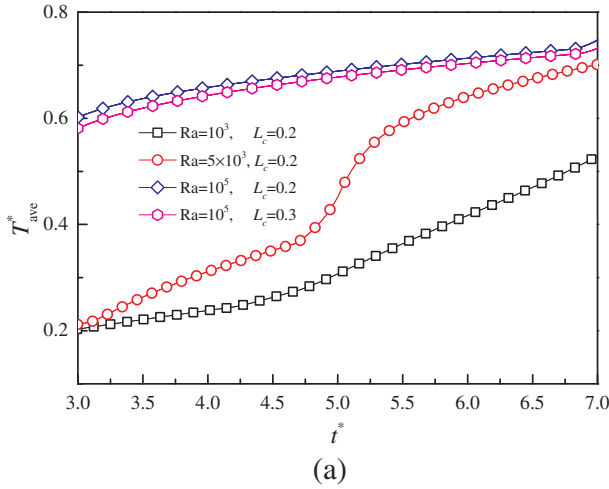
(a)

(b)

Fig. 15. Variations of (a) average temperature and (b) temperature standard deviation with different Rayleigh numbers ($\phi = 0.03$).
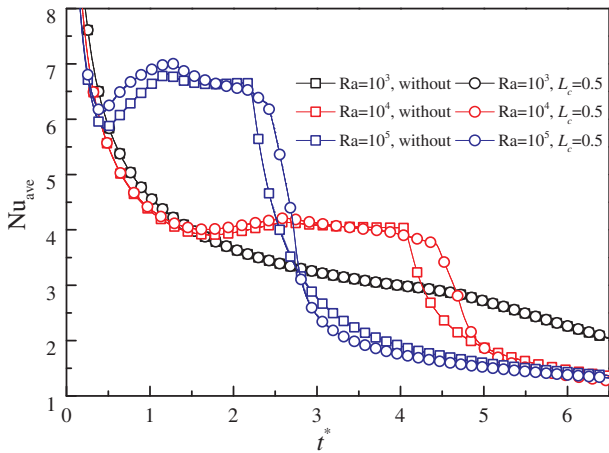

Fig. 16. Variations of average Nusselt number with different Rayleigh numbers ($\phi = 0.03$).

temperature standard deviation), as shown in Figs. 14 and 15(b). Then, more energy is used to transform the NEPCM to liquid phase and the decrement of increasing rate of total liquid fraction in Fig. 13 is put off until $t^* = 6.8$, which results in the coincidence of Ra = 5×10^3 curve and Ra = 10^3 curve (see Fig. 16).

Besides, in Fig. 12, the melting time with $L_c = 0.2$ is smaller than that with $L_c = 0.3$ when the Rayleigh number is 5×10^4 or 10^5.
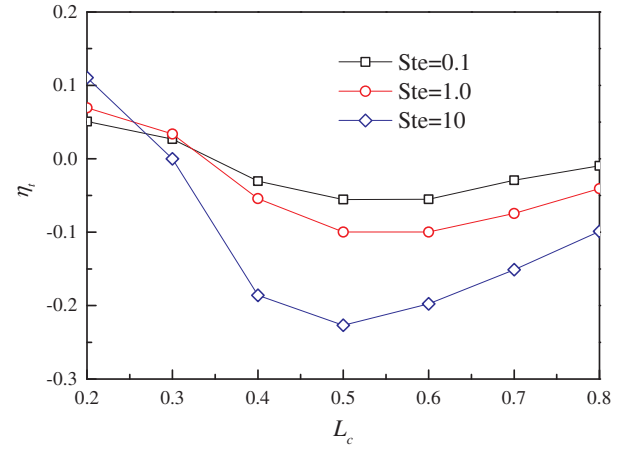

Fig. 17. The relative melting times with different Stefan numbers.

However, when the Rayleigh number is smaller than 5×10^4, the melting time of the case with $L_c = 0.2$ is greater. As shown in Fig. 13, the total liquid fraction with $L_c = 0.2$ is larger than that with $L_c = 0.3$ all the time. The temperature contours at $t^* = 3$ are presented in the latter two images in Fig. 14. When the Rayleigh number is increased from 10^4 to 10^5, the NEPCM in upper part of the cavity melts faster. However, the heat accumulation is stronger and the melting rate of NEPCM in bottom part is slowed down. When the separate plate moves from $L_c = 0.2$ to $L_c = 0.3$ with Ra = 10^3, the temperature distribution becomes more uniform and the heat accumulation is weakened. As a result, the melting process is accelerated. However, as shown in Fig. 15(b), the temperature standard deviation with $L_c = 0.2$ is smaller than that with $L_c = 0.3$ when the Rayleigh number is 10^5. It demonstrates that the heat accumulation with $L_c = 0.3$ is stronger than that with $L_c = 0.2$. Consequently, the melting process is slowed down with Ra = 10^5.

Furthermore, the effects of Stefan number is considered. The Rayleigh number and volume fraction are 10^4 and 0.03, respectively. The relative melting time is defined as follows:

$$\eta_t = \frac{t_m - t_{m0}}{t_{m0}} \tag{47}$$

where the subscript "0" represents the case without separate plate. The relative melting times with different Stefan number are shown in Fig. 17. It is noted that for all the Stefan numbers, the melting rate can be accelerated with $L_c > 0.3$. With $L_c = 0.3$, the relative melting times are -0.055, -0.100 and -0.227 for Stefan numbers of 0.1, 1.0 and 10, respectively. It demonstrates that the larger Stefan number leads to more effects of separate plate on melting process of NEPCM.

4. Conclusions

In this paper, a separate plate is added to the cavity to weaken the heat accumulation in the upper region, in order to enhance the heat transfer. The solid-liquid phase change MRT-LB model is applied to reveal the heat transfer behavior of NEPCM. The Rayleigh number varies from 10^3 to 10^4. The volumes fractions of 0, 0.01 and 0.03, and the Stefan numbers of 0.1, 1.0 and 10 are investigated. The results can be concluded as follows:

(1) For all the volume fractions and Rayleigh numbers, the NEPCM of the case with separate located at the middle of cavity melts most quickly, resulted from the weaken of heat accumulation.
(2) With the separate plate, the temperature of NEPCM distributes more uniform.
(3) When the location of separate is less than 0.3, the melting rate is slowed down compared with the case without separate plate, due to the heat accumulation near the separate plate.

Acknowledgements

References

[1] Mahdi JM, Nsofor EC. Melting enhancement in triplex-tube latent thermal energy storage system using nanoparticles-fins combination. Int J Heat Mass Transf 2017;109:417–27.

[2] Myers PD, Alam TE, Kamal R, Goswami DY, Stefanakos E. Nitrate salts doped with CuO nanoparticles for thermal energy storage with improved heat transfer. Appl Energy 2016;165:225–33.

[3] Teng T-P. Thermal conductivity and phase-change properties of aqueous alumina nanofluid. Energy Convers Manage 2013;67:369–75.

[4] Karaipekli A, Biçer A, Sarı A, Tyagi VV. Thermal characteristics of expanded perlite/paraffin composite phase change material with enhanced thermal conductivity using carbon nanotubes. Energy Convers Manage 2017;134:373–81.

[5] Elbahjaoui R, El Qarnia H. Transient behavior analysis of the melting of nano-particle-enhanced phase change material inside a rectangular latent heat storage unit. Appl Therm Eng 2017;112:720–38.

[6] Mahamudur Rahman M, Hu H, Shabgard H, Boettcher P, Sun Y, McCarthy M. Experimental characterization of inward freezing and melting of additive-enhanced phase-change materials within millimeter-scale cylindrical enclosures. J Heat Transfer 2016;138:072301.

[7] Seddegh S, Wang X, Henderson AD. A comparative study of thermal behaviour of a horizontal and vertical shell-and-tube energy storage using phase change materials. Appl Therm Eng 2016;93:348–58.

[8] Darzi AAR, Farhadi M, Jourabian M, Vazifeshenas Y. Natural convection melting of NEPCM in a cavity with an obstacle using lattice Boltzmann method. Int J Numer Meth Heat Fluid Flow 2013;24:221–36.

[9] Rabienataj Darzi AA, Jourabian M, Farhadi M. Melting and solidification of PCM enhanced by radial conductive fins and nanoparticles in cylindrical annulus. Energy Convers Manage 2016;118:253–63.

[10] Lohrasbi S, Gorji-Bandpy M, Ganji DD. Thermal penetration depth enhancement in latent heat thermal energy storage system in the presence of heat pipe based on both charging and discharging processes. Energy Convers Manage 2017;148:646–67.

[11] Zhu F, Zhang C, Gong X. Numerical analysis and comparison of the thermal performance enhancement methods for metal foam/phase change material composite. Appl Therm Eng 2016;109:373–83.

[12] Huo Y, Rao Z. Lattice Boltzmann simulation for solid–liquid phase change phenomenon of phase change material under constant heat flux. Int J Heat Mass Transf 2015;86:197–206.

[13] Jourabian M, Farhadi M, Sedighi K. On the expedited melting of phase change material (PCM) through dispersion of nanoparticles in the thermal storage unit. Comput Math Appl 2014;67:1358–72.

[14] Fan L-W, Zhu Z-Q, Xiao S-L, Liu M-J, Lu H, Zeng Y, et al. An experimental and numerical investigation of constrained melting heat transfer of a phase change material in a circumferentially finned spherical capsule for thermal energy storage. Appl Therm Eng 2016;100:1063–75.

[15] Godson L, Raja B, Mohan Lal D, Wongwises S. Enhancement of heat transfer using nanofluids—an overview. Renew Sustain Energy Rev 2010;14:629–41.

[16] Feng Y, Li H, Li L, Bu L, Wang T. Numerical investigation on the melting of nanoparticle-enhanced phase change materials (NEPCM) in a bottom-heated rectangular cavity using lattice Boltzmann method. Int J Heat Mass Transf 2015;81:415–25.

[17] Yao F-J, Luo K, Yi H-L, Xie M. Analysis of melting with natural convection and volumetric radiation using lattice Boltzmann method. Int J Heat Mass Transf 2017;112:413–26.

[18] Arıcı M, Tütüncü E, Kan M, Karabay H. Melting of nanoparticle-enhanced paraffin wax in a rectangular enclosure with partially active walls. Int J Heat Mass Transf 2017;104:7–17.

[19] Tasnim SH, Hossain R, Mahmud S, Dutta A. Convection effect on the melting process of nano-PCM inside porous enclosure. Int J Heat Mass Transf 2015;85:206–20.

[20] Al-Jethelah MSM, Tasnim SH, Mahmud S, Dutta A. Melting of nano-phase change material inside a porous enclosure. Int J Heat Mass Transf 2016;102:773–87.

[21] Huang R, Wu H. Phase interface effects in the total enthalpy-based lattice Boltzmann model for solid–liquid phase change. J Comput Phys 2015;294:346–62.

[22] Huang R, Wu H. Total enthalpy-based lattice Boltzmann method with adaptive mesh refinement for solid-liquid phase change. J Comput Phys 2016;315:65–83.

[23] Huo Y, Rao Z. The numerical investigation of nanofluid based cylinder battery thermal management using lattice Boltzmann method. Int J Heat Mass Transf 2015;91:374–84.

[24] Guo Z, Zheng C, Shi B. Non-equilibrium extrapolation method for velocity and pressure boundary conditions in the lattice Boltzmann method. Chin Phys 2002;11:366.

[25] Mencinger J. Numerical simulation of melting in two-dimensional cavity using adaptive grid. J Comput Phys 2004;198:243–64.